

# Assessment of the Mass Loss and Radius Change of 3I/ATLAS Based on Observed Production Rates

Tessa T. Frincke,<sup>1\*</sup> Darryl Z. Seligman,<sup>1</sup>

<sup>1</sup>*Department of Physics and Astronomy, Michigan State University, East Lansing, MI 48824, USA*

2 June 2026

## ABSTRACT

Formed from the debris of planet formation, interstellar comets provide invaluable insights into the chemical compositions of planetary systems outside of our Solar System. Spectroscopic observations of 3I/ATLAS, the third interstellar object, reveal production of numerous volatiles and refractory species throughout its trajectory. In this paper we present a framework to calculate the change in radius of an object on an arbitrary trajectory at any point in its orbit, applicable to any small body experiencing mass-loss. We next provide a comprehensive, machine readable table containing volatile and refractory production rates from all reported observations of 3I/ATLAS pre- and post-perihelion. Applying these equations to 3I/ATLAS, we calculate that it has lost  $\sim 1.05 - 6.56$  meters of its surface during its passage through the Solar System, corresponding to  $\sim 10^9 - 10^{10}$  kg and  $\sim 0.10 - 1.13\%$  of its total mass. These numbers could be lower estimates if the dust-to-gas ratio of its outflow was sustained at a high level. Conservative and optimistic estimates were calculated over a range of heliocentric distances defined by the onset of activity in reported observations and the typical onset of sublimation distance for each species, respectively. The reported production rates combined with the change in radius calculation can be used to estimate subsurface locations of various species within the nucleus of 3I/ATLAS. Post-perihelion measurements of 3I/ATLAS likely originated from layers which still experienced some level of galactic cosmic ray processing.

**Key words:** comets: general – minor planets, asteroids: general – planets and satellites: composition

## 1 INTRODUCTION

3I/ATLAS is the third macroscopic interstellar object to ever be detected in the inner Solar System (Denneau et al. 2025). After traversing the interstellar medium (ISM) for Gyr timescales (Hopkins et al. 2025; Taylor & Seligman 2025), 3I/ATLAS was discovered on UT 2025 July 1 by the The Asteroid Terrestrial-impact Last Alert System (ATLAS) survey at a heliocentric distance of  $\sim 4.5$  au (Tonry et al. 2018). 3I/ATLAS adds to a growing population of interstellar objects including 1I/Oumuamua and 2I/Borisov, discovered in 2017 and 2019, respectively (Williams et al. 2017; Borisov et al. 2019).

Initial observations of 3I/ATLAS identified no significant light curve variation, a reddened spectral slope similar to D-type asteroids, and sustained faint activity confirming the cometary nature of the object (Seligman et al. 2025; Frincke et al. 2026; Puzia et al. 2025; Opitom et al. 2025; Kareta et al. 2025; Belyakov et al. 2025). The first interstellar object, 1I/Oumuamua, exhibited nongravitational acceleration (Micheli et al. 2018) with no visible dust coma and photometric inactivity (Ye et al. 2017; Fitzsimmons et al. 2018; Jewitt et al. 2017; Meech et al. 2017). Conversely, 2I/Borisov, the second interstellar object, demonstrated typical cometary activity (Jewitt & Luu 2019; Hui et al. 2020; Guzik et al. 2020; McKay et al. 2020; Fitzsimmons et al. 2019; Kim et al. 2020; Cremonese et al. 2020;

Yang et al. 2021; Opitom et al. 2019; Kareta et al. 2020; Lin et al. 2020; Xing et al. 2020; Bannister et al. 2020; Bagnulo et al. 2021; Aravind et al. 2021; Deam et al. 2025; Cordiner et al. 2020; Bodewits et al. 2020). Initial observations of 2I/Borisov reported physical properties broadly comparable to solar system comets (Jewitt & Luu 2019; Hui et al. 2020; Guzik et al. 2020). Post-perihelion observations of 2I/Borisov revealed a CO abundance relative to H<sub>2</sub>O higher than typical solar system comets (Bodewits et al. 2020; Cordiner et al. 2020).

Pre-discovery time-series photometry of 3I/ATLAS obtained from several facilities confirmed the onset of activity out to heliocentric distance,  $r_H$ , of  $\sim 6$  au. Ye et al. (2025) reported observations obtained with the Zwicky Transient Facility (ZTF) starting on UT 2025 May 15 which confirmed that 3I/ATLAS was active out to a heliocentric distance of 6.5 au and maintained a persistent dust flow starting at  $\sim 9$  au. Photometry collected with the ATLAS network between UT 2025 March 29 and UT 2025 August 29 tracked pre- and near-discovery brightness evolution of 3I/ATLAS (Tonry et al. 2025). Furthermore, independent analyses of pre-discovery photometry obtained with NASA’s Transiting Exoplanet Survey Satellite (TESS) between UT 2025 May and June suggest 3I/ATLAS may have been active out to a heliocentric distances of  $\sim 6$  au (Feinstein et al. 2025; Martinez-Palomera et al. 2025). Observations of 3I/ATLAS obtained with the NSF-DOE Vera C. Rubin Observatory between

\* E-mail: frincket@msu.edu

UT June 21 and the discovery date of UT 2025 July 1 also confirmed activity at large perihelion distances (Chandler et al. 2025).

Observations of the inbound trajectory of 3I/ATLAS traced the onset of volatile and refractory emission in the coma. For example, Alvarez-Candal et al. (2025) estimated the first pre-perihelion upper limit of H<sub>2</sub>O production to be  $< 9.1 \times 10^{26} \text{ s}^{-1}$  from a detection of OH at 4.42 au; beyond where water ice typically sublimates at  $< 3$  au. H<sub>2</sub>O ice was detected at  $\sim 4$  au from observations obtained by Yang et al. (2025) with the NASA Infrared Telescope Facility (IRTF). Furthermore, Xing et al. (2025) constrained water production rates from UT 2025 July 31 – August 1 and UT 2025 August 18 – 20 at 3.51 au from data obtained with the Ultraviolet/Optical Telescope (UVOT) instrument on the *Neils Gehrels Swift Observatory*. Cordiner et al. (2025) reported detections of water ice and gas emission with the James Webb Space Telescope (JWST) Near Infrared Spectrograph (NIRSPec) on UT 2025 August 6 at 3.32 au. Lisse et al. (2025b) also detected H<sub>2</sub>O gas features at 3.26 au with the Spectro-Photometer for the History of the Universe, Epoch of Reionization, and Ices Explorer SPHEREx spacecraft. In addition to water ice and gas, Cordiner et al. (2025) found the coma is enriched in CO<sub>2</sub> compared to CO and H<sub>2</sub>O. Specifically, Cordiner et al. (2025) measured an unusually high CO<sub>2</sub>/H<sub>2</sub>O mixing ratio compared to solar system comets at the same  $r_H$  of 3.32 au. Lisse et al. (2025a) similarly detected a CO<sub>2</sub> dominated and CO depleted coma from spectrophotometry of 3I/ATLAS obtained with SPHEREx on UT 2025 August 1–15. For further discussion of this behavior in solar system comets see Section 5. Hinkle et al. (2025) estimated an upper limit on a production rate of CO of  $< 1.10 \times 10^{27} \text{ s}^{-1}$  from observations of 3I/ATLAS obtained between UT 2025 July 16–21 with the James Clerk Maxwell Telescope (JCMT). Li et al. (2026a) further contributed to pre-perihelion volatile production rates with detections of OH, CO, HCN, and H<sub>2</sub>O derived from radio observations obtained with the 13.7-meter Millimeter-Wave Telescope from UT 2025 August to September.

CN was detected in the coma of 3I/ATLAS at  $\sim 4.47$  au on UT 2025 July 2–5 contemporaneously by de la Fuente Marcos et al. (2025) and Alvarez-Candal et al. (2025). Subsequent pre-perihelion observations reported pre-perihelion detections of CN emission through UT 2025 September 25 at 1.85 au (Hoogendam et al. 2025a; Rahatgaonkar et al. 2025; Salazar Manzano et al. 2025; Hutsemékers et al. 2026b; Hoogendam et al. 2025b; Medler et al. 2026; Lisse et al. 2026; Paek et al. 2026). Observations obtained on UT 2025 August 8–17 with the 2.4-meter Hiltner and 1.3-meter McGraw-Hill Telescopes of the MDM Observatory revealed the onset of CN emission indicative of strong carbon-chain depletion (Salazar Manzano et al. 2025). Pre-perihelion observations of CN emission demonstrated an overall increase in production rates with decreasing heliocentric distance. Coulson et al. (2025) reported production rates of  $(4.0 \pm 1.7) \times 10^{25} \text{ s}^{-1}$  for hydrogen cyanide (HCN) from observations conducted on UT 2025 August 7 and UT 2025 September 14 with the JCMT. Hinkle et al. (2025) derived a steeper slope for the production of HCN than is typical for solar system comets between 4.01–3.97 au and estimated an upper limit production rate of  $< 1.70 \times 10^{24} \text{ s}^{-1}$ . Roth et al. (2025) found asymmetrical production rates with depleted HCN and enhanced CH<sub>3</sub>OH in the sunward region of the coma from data collected with the Atacama Large Millimeter/Sub-millimeter Array (ALMA) from UT 2025 August 28 to UT 2025 October 1.

Cometary nuclei do not reach sufficient effective temperatures for the direct sublimation of atomic metals. The ubiquitous detection of gaseous metals in the coma of solar system comets like NiI and FeI (hereafter Ni and Fe) is explained by the sublimation or photodissociation of volatile metal bearing carbonyls (Manfroid et al.

2021; Hutsemékers et al. 2026b). In the case of 2I/Borisov, Guzik & Drahus (2021) observed gaseous Ni, and suggested photodissociation of a Ni bearing molecular species as the source of the emission. For 3I/ATLAS, Hutsemékers et al. (2026b) posited that the Ni and Fe gas emission at large  $r_H$  from their observations they obtained with the VLT UV-Visual Echelle Spectrograph (UVES) instrument from UT 2025 August 12 to UT 2025 September 14 are a result of the sublimation of Ni(CO)<sub>4</sub> and Fe(CO)<sub>4</sub> carbonyls. The relatively low sublimation temperatures of these carbonyls provide a mechanism for Ni and Fe release that explains the initially larger abundance ratios of Ni/Fe (Hutsemékers et al. 2026b). Furthermore, Rahatgaonkar et al. (2025) reported a sharp increase in Ni emission at 3.78 au with a constant increase in production rates with decreasing heliocentric distance derived from spectroscopic measurements obtained with the VLT X-Shooter and UVES instruments between UT 2025 July 4 and UT 2025 August 21. Additionally, Hoogendam et al. (2025b) reported detections of Ni and CN with no discernible Fe emission from spectrophotometry collected from UT 2025 July to UT 2025 September with the University of Hawaii 2.2-meter telescope.

Analyses of post-perihelion production rates of volatiles and refractory species in the coma of 3I/ATLAS reveal asymmetries that may be indicative of structural inhomogeneities such as volatile reservoirs in sub-surface layers. Zhao et al. (2026) found the overall trend in the post-perihelion production rates derived for CN, Ni, Fe and H<sub>2</sub>O show shallower declining slopes compared to pre-perihelion detections. From the same data from observations obtained with the Xinglong 2.16-meter and Li-jiang 2.4-meter Telescopes between UT 2025 December 2 and UT 2026 January 20, Zhao et al. (2026) measured production rates that revealed a more enriched C<sub>2</sub> post-perihelion coma. Similarly, Tan et al. (2026) presented observations with the Solar Wind Anisotropies (SWAN) camera on the Solar and Heliosphere Observatory (SOHO) of 3I/ATLAS from UT 2025 November and December that confirmed an asymmetric water production rate pre- and post-perihelion. To illustrate, Combi et al. (2025) derived a near-perihelion water production rate of  $3.17 \times 10^{29} \text{ s}^{-1}$  on UT 2025 November 6 and a reduced rate of  $1 - 2 \times 10^{28} \text{ s}^{-1}$  on UT 2025 December 9 as derived from spectroscopic observations obtained with the SOHO/SWAN instrument. Despite asymmetries in the overall production rate trend with heliocentric distance, Lisse et al. (2026) estimated an H<sub>2</sub>O gas production rate that was  $\sim 40$  times larger than pre-perihelion observations, implying a reservoir of water ice was exposed after perihelion passage. Post-perihelion estimates of the water deuterium-to-hydrogen (D/H) ratio imply that 3I/ATLAS is deuterium enriched and potentially formed in a cold environment at temperatures  $\leq 30$  K (Salazar Manzano et al. 2026; Cordiner et al. 2026).

Post-perihelion abundances reveal a change from H<sub>2</sub>O to CO production as the primary driver of activity in the coma of 3I/ATLAS beyond 3 au (Biver et al. 2026). SPHEREx observations taken at  $r_H = 2-2.2$  au found a higher Q(CO)/Q(H<sub>2</sub>O) ratio of 0.55 compared to Q(CO<sub>2</sub>)/Q(H<sub>2</sub>O) ratio of 0.23 (Lisse et al. 2026) indicative of a CO-dominated coma. Furthermore, Shinnaka et al. (2026) estimated that the abundance ratio of CO<sub>2</sub>/H<sub>2</sub>O decreased since pre-perihelion measurements. Roth et al. (2026) reported CO as the most abundant species detected from a spatial-spectral mapping from observations obtained UT 2025 December 22-23 utilizing the JWST NIRSpec Integral Field Unit (IFU). An analysis of isotopic abundances found an unusually large <sup>12</sup>C/<sup>13</sup>C ratios compared to solar system comets including 141 – 191 for CO<sub>2</sub> and 123–172 for CO ratios (Cordiner et al. 2026). Opitom et al. (2026) reported a similarly abundant <sup>12</sup>C/<sup>13</sup>C ratio of 147 as well as a nitrogen isotopic ratio of <sup>14</sup>N/<sup>15</sup>N = 343

which is about two times larger than typical Solar System comet abundances.

Further detections of volatiles and refractory species offer insights into the formation location and trace the evolution of post-perihelion activity of 3I/ATLAS. Medler et al. (2026) reported pre- and post-perihelion spectroscopic measurements of 3I/ATLAS spanning from UT 2025 July to November that show CN emission and are suggestive of a different formation location than 2I/Borisov. Hutsemékers et al. (2026a) tracked the post-perihelion Ni and Fe emission from 3I/ATLAS using the UVES instrument on the VLT spanning from UT 2025 December 4 to UT 2026 February 22 and reported a more gradual decrease in production rates. Hoogendam et al. (2026) reported production rates of Ni, Fe, CN, C<sub>2</sub>, and C<sub>3</sub> derived from IFU spectroscopic measurements of 3I/ATLAS taken with the Keck Cosmic Web Imager (KCWI) on UT 2025 November 16. Belyakov et al. (2026) revealed the first detection of CH<sub>4</sub> and a reduction in overall outgassing from spectroscopic measurements of 3I/ATLAS obtained with *JWST* Mid-Infrared Instrument (MIRI) on UT 2025 December 15–16 and 27.

Interstellar objects in general and 3I/ATLAS specifically offer the opportunity to potentially measure the chemical composition of primordial planetary building blocks. However, 3I/ATLAS may have undergone extreme processing by galactic cosmic rays over ~ Gyrs in the ISM before being detected in the inner Solar System, which would have altered its composition, similar to mechanisms invoked to explain 1I/'Oumuamua's acceleration (Bergner & Seligman 2023). Maggiolo et al. (2025) posited that 3I/ATLAS was processed via radiolytic conversion of CO to CO<sub>2</sub> by galactic cosmic rays (GCR) in the ISM down to a depth of ~ 15–20 m (see also Gronoff et al. 2020; Maggiolo et al. 2020). For a more in-depth discussion of the GCR processing of the surface layers of comets see Section 5. Specific formation pathways of 3I/ATLAS may have lead to the asymmetry in CO<sub>2</sub> and CO as activity drivers pre- and post-perihelion (Harrington Pinto et al. 2022; A'Hearn et al. 2012). The derived kinematic age of ~ 3–11 Gyr (Taylor & Seligman 2025) and inferred isotopic age of 11–12 Gyr (Cordiner et al. 2026) of 3I/ATLAS emphasizes the need to address the potential for surface processing in the ISM after formation. Therefore, estimates of surface erosion are vital to determine the observability of minimally processed materials in the coma from sublimation driven activity of 3I/ATLAS outlined above.

Additional observational analyses of 3I/ATLAS are cited here for completion including photometry, polarimetry, spectrophotometry, radio searches, and dust mass-loss and radius constraints (Beniyama 2025; Gray et al. 2025; Jewitt et al. 2025; Santana-Ros et al. 2025; Jewitt & Luu 2025; Hartman et al. 2026; Serra-Ricart et al. 2025; Gillan et al. 2026; Ren et al. 2026; Zhang & Battams 2026; Eubanks et al. 2025b; Trigo-Rodríguez et al. 2025; Li et al. 2026b; Jacobson-Bell et al. 2025; Sheikh et al. 2025; Hui et al. 2026; Martinez-Palomera et al. 2026; Choi et al. 2026). We also cite theoretical analyses relevant to 3I/ATLAS (Ahuja & Ganesh 2026; Forbes & Butler 2026; Monk & Seligman 2026; Spada et al. 2026; Ferrin et al. 2026; Yaginuma et al. 2025a; Grant & Jones 2025; Pérez-Couto et al. 2025; Guo et al. 2025; Eubanks et al. 2025a; Yaginuma et al. 2025b; Hopkins et al. 2025; Keto & Loeb 2026).

The paper is organized as follows: in Section 2, we present a methodology for estimating the change in nuclear radius of any small body for an arbitrary orbit and mass loss rate. In Section 3, we provide a summary of production rates of volatiles and refractory species from all reported pre- and post-perihelion measurements. In Section 4, we estimate the change in radius of 3I/ATLAS over its trajectory in the Solar System and provide a table of mass loss derived over conservative and optimistic ranges in position and the

contributions of certain volatile species. In Section 5, we discuss the results and summarize our conclusions in Section 6.

## 2 CHANGE IN RADIUS FOR ARBITRARY ORBIT AND MASS LOSS FUNCTION

In this section we present a methodology to estimate the change in radius of a small body experiencing mass-loss at an arbitrary location of an arbitrary orbit. This methodology is useful for quantifying the erosion of processed layers from the surface of 3I/ATLAS. This calculation assumes a spherically symmetric geometry for the nucleus, but could be updated to arbitrary shapes in future work.

### 2.1 Change in Radius Formulation

We assume that the mass loss rate is directly proportional to the rate of change of the volume of the nucleus. The mass loss rate,  $\dot{m}$ , for the generic small body is then:

$$\dot{m} = \rho \frac{dV}{dt}. \quad (1)$$

In Equation (1),  $\rho$  is the bulk density of the nucleus. Assuming a spherical geometry for the nucleus, the volume,  $V$ , and the rate of change of the volume are given by,

$$\frac{dV}{dt} = 4\pi R^2 \frac{dR}{dt}. \quad (2)$$

In Equation (2),  $R$  is the radius of the nucleus. Substituting Equation (2) into Equation (1) gives the rate of change of the nuclear radius during its passage in the Solar System as,

$$\frac{dR}{dt} = \dot{m} \left| 4\pi R^2 \rho \right|. \quad (3)$$

After separation of variables and integration, we solve for the reduction of radius with time given as,

$$R_f = \left( R_0^3 + (3\dot{m}\Delta\tau) \right) \left( 4\pi\rho \right)^{\frac{1}{3}}. \quad (4)$$

In Equation (4),  $R_0$  is the initial nuclear radius at some initial time,  $\tau_0$ , and  $R_f$  is the radius at some later time,  $\tau_f$ . Here we assume that  $\dot{m}$  remains constant for simplicity; later we will introduce more complex mass loss functions to the derivation that can be applied more generally.

Small bodies with smaller initial radii exhibit significant radius loss. Moreover, the overall change in radius is extremely sensitive to the initial radius of the object. This sensitivity is visualized in Figure 1 where the change in radius,  $\Delta R$ , is computed using Equation 4 over a range of total change in mass,  $\Delta m$ , values and initial comet radius,  $R_0$ . The dashed line separates the regime of mass loss and initial radii over which the change in radius is equal to the initial radius, indicative of complete disintegration of the nucleus.

### 2.2 Change in Radius with Constant Mass

Here we calculate the change in radius at an arbitrary position,  $r$ , in its orbit. To achieve this, we calculate a solution, similar to Equation (4), for the nuclear radius at a given true anomaly for a small body in either a circular, eccentric, or hyperbolic orbit. The velocity vector,  $\dot{\mathbf{r}}$ , and angular momentum vector,  $\mathbf{h}$ , assuming a two-body system are given as,

$$\dot{\mathbf{r}} = \dot{r}\hat{\mathbf{r}} + r\dot{\theta}\hat{\boldsymbol{\theta}}, \quad (5)$$

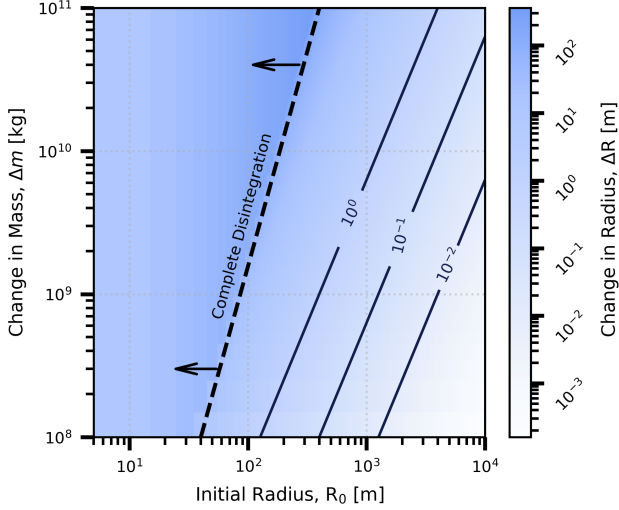


**Figure 1.** The change in radius of a small body sensitively depends on its initial radius. Small bodies with larger initial radii require significant mass loss to have appreciable nuclear erosion. Contour lines indicate constant change in radius given a constant total change in mass,  $\Delta m$ , and initial radius,  $R_0$ . The area left of the dashed line indicates the regime where the object loses all of its mass.

and

$$\mathbf{h} = \mathbf{r} \times \dot{\mathbf{r}} = r^2 \dot{\theta}. \quad (6)$$

In Equation (6),  $\theta$  is the true anomaly. The position of the small body in its orbit is determined by:

$$r(\theta) = \frac{p}{1 + e \cos \theta}. \quad (7)$$

In Equation (7),  $p$  is the semilatus rectum and  $e$  is the eccentricity of the object. Rearranging Equation (6) gives  $\dot{\theta} = h/r^2$ , where the magnitude of the angular momentum vector is defined as  $h = \sqrt{p\mu}$  and  $\mu$  is the equation of relative motion between two bodies. The differential equation relating change in radius to the change in true anomaly is given by,

$$\frac{dR}{d\theta} = \frac{\dot{m}}{4\pi\rho} \frac{r^2}{h}. \quad (8)$$

Therefore, the radius change can generically be calculated using:

$$\int_{R_0}^{R_f} R^2 dR = \int_{\theta_0}^{\theta_f} \left( \frac{\dot{m}}{4\pi\rho} \frac{r^2}{h} \right) d\theta. \quad (9)$$

In Equation (9) we assume that  $\theta_0$  and  $\theta_f$  span some range of true anomaly over which the final nuclear radius will be evaluated.

### 2.2.1 Circular Orbit

For the circular orbit with  $e = 0$ , Equation (7) reduces to  $r = a$ , where  $a$  is the semi-major axis of the orbit. Integrating Equation (9) gives the solution for the radius for a circular orbit with a generic constant mass loss function  $\dot{m}$  as,

$$R_f = \left[ R_0^3 + \dot{m} \left( \frac{3a^2}{4\pi\rho h} \right) \theta \right]^{\frac{1}{3}}. \quad (10)$$

### 2.2.2 Eccentric Orbit

For the eccentric orbit case where  $0 < e < 1$ , Equation (7) does not reduce and is substituted directly into Equation (9) with  $p = a(1 - e^2)$ ,

$$\int_{R_0}^{R_f} R^2 dR = \int_0^\theta \left( \frac{h^3}{\mu^2} \frac{\dot{m}}{4\pi\rho} \right) \frac{d\theta}{(1 + e \cos \theta)^2}. \quad (11)$$

Equation (11) gives the solution for the final radius over a given range of true anomaly from perihelion passage as,

$$R_f = \left[ R_0^3 - \left( \frac{h^3}{\mu^2} \frac{3\dot{m}}{4\pi\rho} \right) \frac{1}{(1 - e^2)^{\frac{3}{2}}} \times \left( 2 \arctan \sqrt{\frac{1 - e}{1 + e}} \tan \left( \frac{\theta}{2} \right) - \frac{e \sqrt{1 - e^2} \sin \theta}{1 - e \cos \theta} \right) \right]^{\frac{1}{3}}. \quad (12)$$

### 2.2.3 Hyperbolic Orbit

Similarly, for a hyperbolic trajectory where  $e > 1$ , Equation (11) is used with  $p = a(e^2 - 1)$  instead. The angle between incoming and outgoing asymptotes of the hyperbolic trajectory as  $r$  approaches infinity,  $\theta_{min}$  and  $\theta_{max}$ , define the bounds of integration. The maximum angle is derived from the limits of Equation (8) and is defined as,

$$\theta_{max} = 2 \cos^{-1} \left( -\frac{1}{e} \right). \quad (13)$$

The solution to integration from perihelion to a given true anomaly gives the final radius through a given range of true anomaly for a small body on a hyperbolic trajectory:

$$R_f = \left[ R_0^3 - \left( \frac{h^3}{\mu^2} \frac{3\dot{m}}{4\pi\rho} \right) \frac{1}{e^2 - 1} \left[ \frac{e \sin \theta}{1 + e \cos \theta} - \frac{1}{\sqrt{e^2 - 1}} \times \ln \left( \frac{\sqrt{e + 1} + \sqrt{e - 1} \tan \frac{\theta}{2}}{\sqrt{e + 1} - \sqrt{e - 1} \tan \frac{\theta}{2}} \right) \right] \right]^{\frac{1}{3}}. \quad (14)$$

Solar System comets with larger eccentricities and smaller semi-major axes experience more relative mass loss on average over a single orbit. In Figure 2 we show the orbits of Solar System comets queried from JPL Small-Body Database (Giorgini et al. 2015) plotted with contours as lines of constant orbit-averaged dimensionless mass loss using these equations.

## 2.3 Change in Radius with Inverse Square Law Mass Loss Function

Here we present solutions for the erosion of the surface of small body on a circular, eccentric, or hyperbolic orbit assuming an inverse square mass loss given as,

$$\dot{m} = A (r^{-2}). \quad (15)$$

In Equation (15),  $A$  is a constant mass loss coefficient.

### 2.3.1 Circular Orbit

For a circular orbit, the mass loss of a nucleus is defined as  $\dot{m} = A/a^2$ , and substituting into Equation (10) for  $\dot{m}$  gives,

$$R_f = \left[ R_0^3 - \left( \frac{3A}{4\pi\rho h} \right) \theta \right]^{\frac{1}{3}}. \quad (16)$$

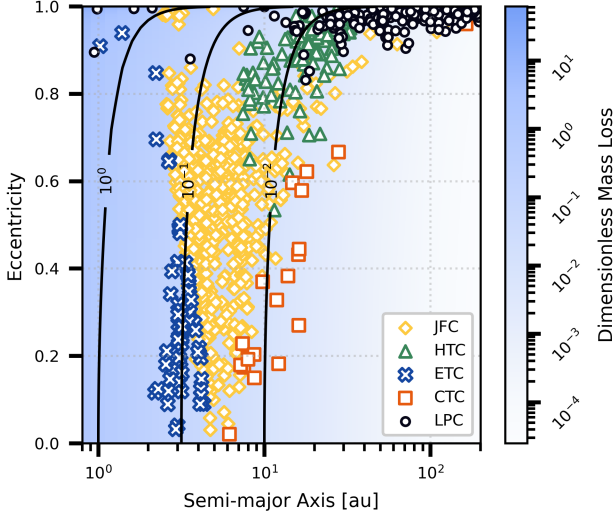


**Figure 2.** Solar System comets with larger eccentricities and smaller semi-major axes exhibit more mass loss over a single orbit. Contours are lines of constant orbit-averaged dimensionless mass loss. Jupiter-Family Comets (JFC) are represented as diamonds, Halley-Type Comets (HTC) as triangles, Encke-Type Comets (ETC) as crosses, and Chiron-Type Comets (CTC) as squares, and Long-Period Comets (LPC) or other as circles.

### 2.3.2 Eccentric Orbit

For an eccentric orbit, the final radius is similarly calculated using a mass loss rate,

$$\dot{m} = A \left( \frac{(1 + e \cos \theta)^2}{a^2(1 - e^2)^2} \right). \quad (17)$$

The final radius can be calculated using,

$$R_f = \left[ R_0^3 - \left( \frac{3A}{4\pi\rho h_{ecc}} \right) \theta \right]^{\frac{1}{3}}. \quad (18)$$

In Equation (18) the magnitude of angular momentum  $h_{ecc}$ , is defined as:

$$h_{ecc} = \sqrt{a(1 - e^2)}\mu. \quad (19)$$

### 2.3.3 Hyperbolic Orbit

And finally for a hyperbolic trajectory the inverse square mass loss function is,

$$\dot{m} = A \left( \frac{(1 + e \cos \theta)^2}{a^2(e^2 - 1)^2} \right). \quad (20)$$

The final radius for a hyperbolic trajectory is given as the same solution as for an eccentric orbit in Equation (18), but  $h$  is instead defined as,

$$h_{hyp} = \sqrt{a(e^2 - 1)}\mu. \quad (21)$$

## 2.4 Change in Radius with Arbitrary Power Law Mass Loss Function

Here we present solutions with an arbitrary mass loss defined by an inverse power law with an arbitrarily defined power index,  $\beta$ ,

$$\dot{m} = A(r^{-\beta}). \quad (22)$$

### 2.4.1 Circular Orbit

For a circular orbit the generic mass loss function assuming an inverse power law is defined as  $\dot{m} = A/a^\beta$ . This mass loss function gives a solution for the final radius of the nucleus of a small body in a circular orbit with a give power law dependency given as,

$$R_f = \left[ R_0^3 - \frac{A}{a^\beta} \left( \frac{h^3}{\mu^2} \frac{3}{4\pi\rho} \right) \theta \right]^{\frac{1}{3}}. \quad (23)$$

### 2.4.2 Eccentric Orbit

The mass loss function for an eccentric orbit of an arbitrary power law is,

$$\dot{m} = A \left( \frac{a(1 - e^2)}{1 + e \cos \theta} \right)^{-\beta}. \quad (24)$$

The solution of the final radius through a given range of true anomaly for an eccentric orbit is defined as,

$$\int_{R_0}^{R_f} R^2 dR = \left( \frac{h^3}{\mu^2} \frac{A}{4\pi\rho} \right) \int_0^\theta \left( \frac{a(1 - e^2)}{1 + e \cos \theta} \right)^{-\beta} \frac{d\theta}{(1 + e \cos \theta)^2}. \quad (25)$$

### 2.4.3 Hyperbolic Orbit


The mass loss for a small body on a hyperbolic trajectory is given as,

$$\dot{m} = A \left( \frac{a(e^2 - 1)}{1 + e \cos \theta} \right)^{-\beta}. \quad (26)$$

Finally, the final nuclear radius over a range of true anomaly for a hyperbolic orbit with an arbitrary power law index is,

$$\int_{R_0}^{R_f} R^2 dR = \left( \frac{h^3}{\mu^2} \frac{1}{4\pi\rho} \right) \int_0^\theta \left( \frac{a(e^2 - 1)}{1 + e \cos \theta} \right)^{-\beta} \frac{d\theta}{(1 + e \cos \theta)^2}. \quad (27)$$

## 3 ESTIMATES OF 3I/ATLAS PRODUCTION RATES

In this section we synthesize the production rates of volatiles and refractory compounds detected in the coma of 3I/ATLAS. We collect all published production rates, denoted as  $Q$ , for 3I/ATLAS and provide them in Table A1 along with the corresponding heliocentric distance/s,  $r_H$ , observation date/s, facility/instrument, and relevant citation. A machine readable version of this table is also provided in the accompanying GitHub .

To ascertain the contribution of each chemical species to the overall activity throughout the trajectory of 3I/ATLAS, we fit the production rates as a function of heliocentric distance,  $r_H$ , separately for pre- and post-perihelion. We require at least four reported production rates as criteria for fitting for a specific species. With that criteria, we are able to fit nine pre-perihelion and seven post-perihelion chemical species. We perform these fits for each species for pre- and post-perihelion rates, separately to capture differences in trends before and after perihelion passage. We use the `scipy.optimize.curve_fit` which performs a non-linear least-squares to fit the function,

$$\ln(Q_X) = -\beta \ln(r) + b. \quad (28)$$

**Table 1.** Power law indices,  $\beta$ , relating published production rates for 3I/ATLAS reported in A1 to position or heliocentric distance,  $r_H$ , for pre- and post-perihelion. Columns  $m_{\text{pre, con}}$  and  $m_{\text{pre, opt}}$  are the conservative and optimistic estimates for total mass loss estimates, respectively, from pre-perihelion observations. Similarly for post-perihelion observations  $m_{\text{post, con}}$  and  $m_{\text{post, opt}}$  are the conservative and optimistic estimates for total mass loss. Entries with dashes indicate insufficient data to determine a reliable fit. All total mass loss values  $m$  are listed as a factor of  $10^6$  kg.

Volatile	$\beta_{\text{pre}}$	$m_{\text{pre, con}}$ $10^6$ [kg]	$r_H^{\text{pre, con}}$ (au)	$m_{\text{pre, opt}}$ $10^6$ [kg]	$r_H^{\text{post, opt}}$ [au]	$\beta_{\text{post}}$	$m_{\text{post, con}}$ $10^6$ [kg]	$r_H^{\text{post, con}}$ [au]	$m_{\text{post, opt}}$ $10^6$ [kg]	$r_H^{\text{post, opt}}$ [au]
H <sub>2</sub> O	(5.729 ± 1.876)	494.78	4.41–1.96	2833.76	4.41–1.35	(8.110 ± 0.722)	301.0	1.37–2.54	3400.0	1.35–4.41
CO <sub>2</sub>	—	—	—	—	—	(-1.242 ± 4.299)	281.0	2.08–2.40	42171.10	1.35–12.25
CO	(4.030 ± 3.585)	186.57	3.92–2.01	711.0	23.3–1.35	(1.300 ± 1.011)	574.0	1.36–2.39	2265.0	1.35–23.30
CN	(4.466 ± 0.594)	1.88	4.47–1.85	5.66	5.02–1.35	(2.674 ± 0.724)	2.86	1.50–3.29	3.89	1.25–5.02
HCN	(0.996 ± 1.218)	1.79	4.01–2.19	3.36	4.60–1.35	—	—	—	—	—
OH	(1.514 ± 1.716)	84.4	4.41–2.19	159.0	4.41–1.35	—	—	—	—	—
Ni	(6.863 ± 0.386)	0.155	3.78–1.85	0.977	3.78–1.35	(6.170 ± 1.011)	0.284	1.50–3.85	0.413	1.35–7.84
Fe	(13.064 ± 0.420)	0.0423	2.64–1.85	1.94	3.25–1.35	(9.323 ± 0.838)	0.528	1.50–3.50	1.94	1.35–12.26
C <sub>2</sub>	(6.179 ± 1.066)	0.606	2.64–1.85	3.52	3.00–1.35	(8.833 ± 0.480)	1.03	1.50–2.57	2.36	1.35–3.0
CH <sub>3</sub> OH	(9.120 ± 1.023)	81.0	2.64–1.71	557.0	3.7–1.35	—	—	—	—	—
Total		851.30		4276.27			4726.9		52124.7	

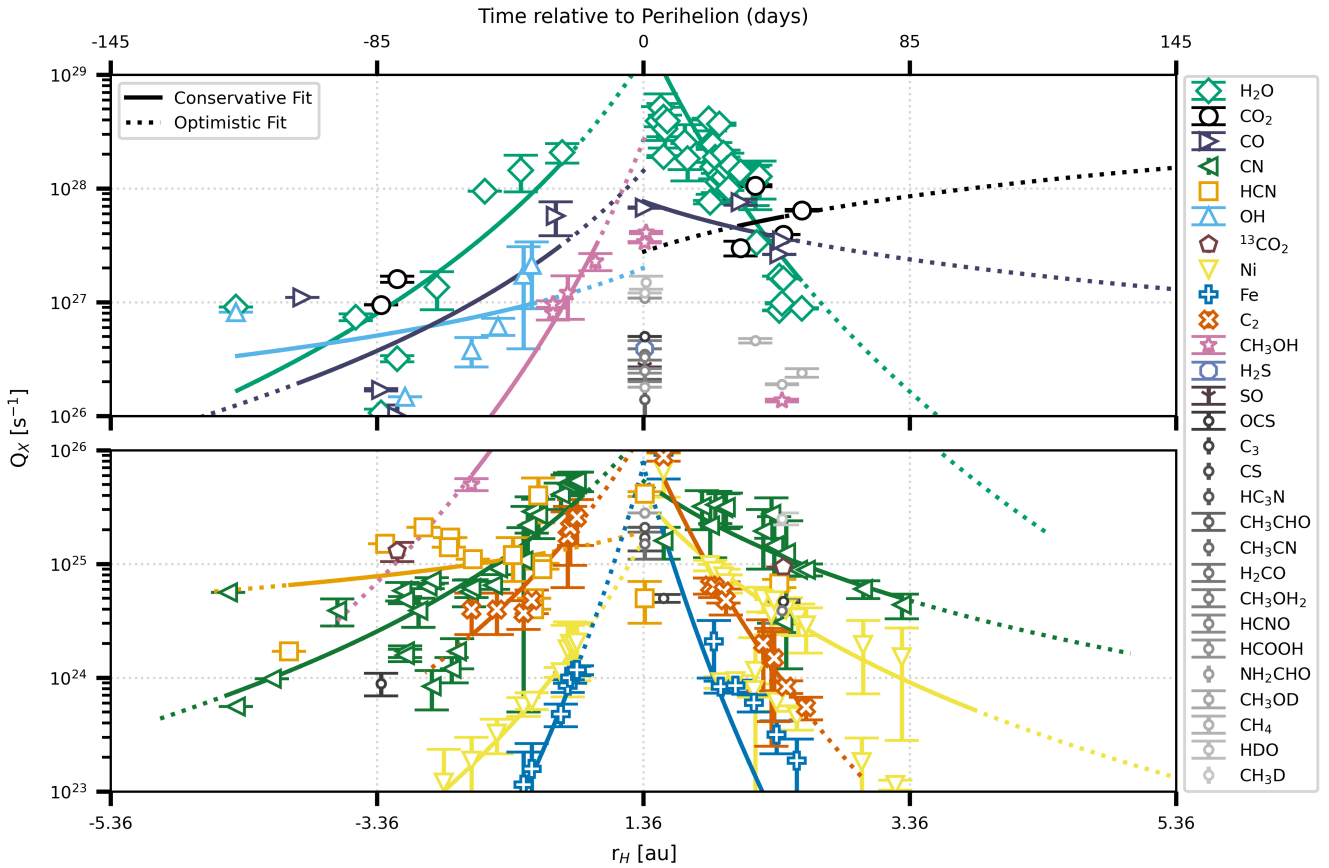


**Figure 3.** Pre- and post-perihelion production rates for all reported chemical species outgassed by 3I/ATLAS as function of heliocentric distance and time relative to perihelion passage  $q \sim 1.36$  au. Pre-perihelion heliocentric distances are signed to visualize the inbound trajectory. Conservative and optimistic production rate fits are visualized as solid and dotted lines, respectively. Upper limits are indicated as points without error bars.

In Equation (28),  $\beta$  is the power-law index and  $b$  is the intercept (Virtanen et al. 2020). These parameters are estimated from Equation (28) for the production rate as a function of position.

For each species we estimate a conservative and optimistic fit for both pre- and post-perihelion measurements. The conservative fits are defined only between the first and last measurement of that

species. Optimistic fits are defined over the entire trajectory interior to the relevant sublimation front. In other words, the conservative fits assume 3I/ATLAS was active during the observations, while the optimistic fits assume 3I/ATLAS was active out to large distances. The results of each fit, and resulting mass loss calculated in the next section are provided in Table 1.

Sublimation fronts/snowline positions for chemical species for which sublimation is the primary mechanism for transition to a gaseous phase were estimated from sublimation temperatures collected from the NIST Chemistry WebBook (Linstrom & Mallard 2001). For certain chemical species for which sublimation is not the primary mechanism or were not available on the NIST Chemistry WebBook (Linstrom & Mallard 2001), the upper limit of the optimistic fits were determined from literature values (Gerakines et al. 2024; Al Mawla et al. 2025; Kushwaha et al. 2025; Helbert et al. 2005; Lucas et al. 2005). The upper limits on optimistic fits for Ni and Fe were derived from estimated sublimation temperatures for the  $\text{Fe}(\text{CO})_4$  and  $\text{Ni}(\text{CO})_4$  carbonyls which are 97 – 108 K and 74 – 82 K, respectively (Manfroid et al. 2021). We note that the optimistic range for  $\text{H}_2\text{O}$  we define extends beyond the typical snowline of  $\sim 3$  au due to reported upper limit of  $\text{H}_2\text{O}$  productions out to 4.41 au (Alvarez-Candal et al. 2025). The position of sublimation fronts are reported in Table 1.

The power-law index parameter  $\beta$  for the conservative and optimistic production rate fits for each chemical species are provided in Table 1 and are arranged by pre- and post-perihelion measurements. We emphasize that the fits are determined with discontinuous observational data and are meant to be interpreted as an approximation of the overall evolution of the production rates throughout the trajectory of 3I/ATLAS. Moreover, upper limits are treated as values in the fits. Due to the sparseness of the data, some power law indices indicate a decreasing production rate approaching perihelion distance or vice-versa. These particular power law indices are negative in Table 1 and entries with dashes indicate that there was insufficient data to obtain a reliable fit.

Conservative and optimistic fits are plotted in Figure 3 along with the reported production rates as function of heliocentric distance signed relative to perihelion and days relative to perihelion. The calculated production rate of  $\text{H}_2\text{O}$  has a steeper power law on the outbound trajectory of 3I/ATLAS contrary to other analyses that found a shallower declining slope than pre-perihelion Zhao et al. (2026); Tan et al. (2026). Similarly, there is a steeper decreasing slope for post-perihelion  $\text{C}_2$  confirming estimates made by Zhao et al. (2026). Overall these calculations produced shallower slopes for CO, CN, Ni, and Fe that are indicative of a more gradual decrease in production as 3I/ATLAS moves out to larger heliocentric distances. Of these asymmetries we note that CO and Fe demonstrate appreciably shallower slopes compared to pre-perihelion production. Asymmetric CO production in pre- and post-perihelion observations of 3I/ATLAS may be indicative of the change from a  $\text{CO}_2$  (Cordiner et al. 2025; Lisse et al. 2025a) to CO (Lisse et al. 2026; Shinnaka et al. 2026; Roth et al. 2026) dominated coma. This cannot be confirmed without further data, and therefore more conclusive fit to pre-perihelion  $\text{CO}_2$  production rates. HCN and OH appear to have the most gradual increase in production on the inbound trajectory of 3I/ATLAS whereas  $\text{CH}_3\text{OH}$  and Fe production rates increase sharply approaching perihelion distance.

#### 4 3I/ATLAS MASS LOSS AND RADIUS CHANGE

In an effort to contextualize the chemical evolution of the outgassing detected in observations of 3I/ATLAS we estimate the depth down to which the nucleus has eroded in this section. In Subsection 4.1 we estimate the mass loss based on the best fitting production rate power laws derived in the previous section. In Subsection 4.2 we estimate the corresponding change in radius.

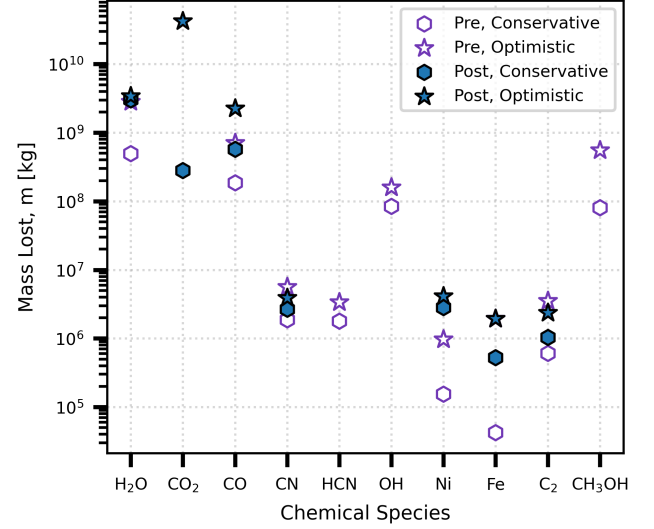


**Figure 4.** Production of gaseous  $\text{H}_2\text{O}$ ,  $\text{CO}_2$ , and  $\text{CO}$  dominated pre- and post-perihelion mass loss. Hexagon markers indicated conservative mass loss. Star markers indicate optimistic mass loss estimates. Unfilled and filled markers are pre- and post-perihelion mass loss estimates, respectively.

##### 4.1 Mass Loss Estimate

To determine change in nuclear radius we first use the interpolated production rates estimated in Section 3 to estimate the cumulative mass loss at each position in the trajectory of 3I/ATLAS. We calculate the mass loss rate  $\dot{m}$  for each chemical species from pre- and post-perihelion fits to production rates given as,

$$\dot{m} = Q_X M_X N_A, \quad (29)$$

In Equation (29),  $Q_X$  is the production rate,  $M_X$  is the molar mass, and  $N_A$  is Avogadro’s number. This provides the mass loss rate in  $\text{kg s}^{-1}$  at each position over the range of heliocentric distances defined by conservative and optimistic fits for each chemical species.

We integrate these mass loss rates to calculate conservative and optimistic estimates of the total mass lost from the outgassing from each chemical species and provide those along with the corresponding fit parameters in Table 1. We estimate the total pre- and post-perihelion mass loss to be  $\sim 10^8$ – $10^9$  kg and  $\sim 10^9$ – $10^{10}$  kg, respectively. The total estimated mass loss from outgassing over the entire trajectory of 3I/ATLAS through the inner Solar System is  $\sim 10^9$ – $10^{10}$  kg. In Figure 4 we show all of these mass loss estimates to visualize the contribution of each species to pre- and post-perihelion mass loss. Assuming a density of a typical comet of  $0.5 \text{ g cm}^{-3}$  and a radius of  $1.3 \pm 0.2$  km estimated for 3I/ATLAS by Hui et al. (2026),  $\sim 0.10$ – $1.13\%$  of the comet’s total mass was lost from outgassing.

$\text{H}_2\text{O}$  production dominated the mass loss in pre-perihelion estimates while CO,  $\text{H}_2\text{O}$ , and  $\text{CO}_2$  contribute the most to post-perihelion mass loss. Following the production rate asymmetries discussed in Section 3, CO shows an evident increase in overall contribution to the total mass loss after perihelion passage. Broadly, contribution from CN, Ni, Fe, and  $\text{C}_2$  to the total mass loss decreased post-perihelion.

##### 4.2 Nucleus Erosion Estimate

We estimate the depth down to which the surface of 3I/ATLAS has been eroded at each position throughout its trajectory. We utilize

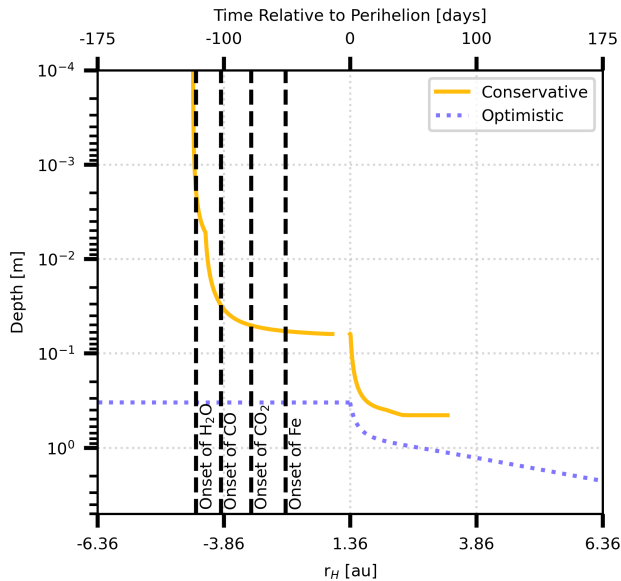


**Figure 5.** Depth of erosion into 3I/ATLAS as a function of heliocentric distance and time relative to perihelion, where smaller depths are closer to the surface. The conservative and optimistic depth estimates are shown as solid and dotted lines, respectively. The vertical dashed lines indicate the heliocentric distances of the first detections of H<sub>2</sub>O, CO, CO<sub>2</sub>, and Fe, respectively.

the mass loss rates calculated in Section 4.1 and Equation (21) to determine the final radius for a hyperbolic orbit at each position in the trajectory of 3I/ATLAS. For this calculation we assume a typical comet density of  $0.5 \text{ g cm}^{-3}$ , initial radius of 1.3 km (Hui et al. 2026), and the mass loss rates over the same conservative and optimistic ranges of heliocentric distance outlined in Table 1. With these final radii we can determine the change in radius to ascertain the cumulative erosion at each position. This radius change estimate assumes that the contribution of dust to the total mass loss budget was negligible.

Depth estimates are plotted in Figure 5 as a function of heliocentric distance  $r_H$  and time relative to perihelion. Negative  $r_H$  and time indicate the inbound trajectory of 3I/ATLAS and days before perihelion passage, respectively. The depth calculations made with conservative and optimistic mass loss estimates are represented as solid and dotted lines, respectively. Here smaller depths are indicative of less erosion and are closer to the surface or initial radius of 3I/ATLAS. The vertical dashed lines indicate the heliocentric distances at which the first detections of H<sub>2</sub>O, CO, CO<sub>2</sub>, and Fe were made from reported observations. To visualize the onset of these volatiles the full range of the optimistic depth estimates are not shown.

We find an approximate erosion down to  $\sim 0.10$ – $1.18$  meters from pre-perihelion outgassing and final depth estimate after post-perihelion outgassing of  $\sim 1.05$ – $6.56$  meters. These depth estimates comprise 0.08–0.50% of the assumed 1.3 km initial radius. We notice an initial increase in depth after the first detections of H<sub>2</sub>O that is consistent with H<sub>2</sub>O and CO dominating the total pre-perihelion mass loss.

## 5 DISCUSSION

In this paper, we estimate the mass loss and corresponding change in radius of 3I/ATLAS as a result of the outgassing of chemical species down to a depth of  $\sim 1.05$ – $6.56$  meters. We provide a method to estimate the change in radius of any small body that is losing mass through a given orbit. We collate a comprehensive table of all available production rates from all chemical species detected in the coma of 3I/ATLAS in Table A1. We also provide a full length machine readable version of Table A1 for the community to reference. In addition to erosion estimates, we estimate the mass loss throughout the comet’s trajectory and provide a table with the contribution of certain chemical species over different ranges of heliocentric distances.

Certain fits to production rates found in this work differ from other published analyses largely due to the difference in quantity of data and/or method for obtaining fit parameters. The derived fits do not encapsulate the entire inventory of chemical species in the coma of 3I/ATLAS at each point in the comet’s trajectory due to the sparseness of the data. We therefore present the erosion and mass loss calculations as approximations. With these approximations we attempt to contextualize the presence of certain volatile species and the significance of processing down into deeper layers of the nucleus. Moreover, our mass loss estimate assumed that the contribution of dust to the total mass loss budget was negligible. If the dust-to-gas ratio was larger than that in typical solar system comets, then the estimates of the mass loss and radius change would be enhanced by a similar factor.

The activity for most solar system comets is primarily driven by the sublimation of H<sub>2</sub>O, CO, and CO<sub>2</sub> ices for which abundances provide insights into the formation of the early Solar System (Jewitt 2009). Of particular interest are CO and CO<sub>2</sub> which drive activity of comets at relatively large heliocentric distances due to their low sublimation temperatures. Harrington Pinto et al. (2022) presented a survey compiling production rates of CO and CO<sub>2</sub> for 25 solar system comets and categorized them based on which volatile dominates the activity. Harrington Pinto et al. (2022) demonstrated that dynamically new LPCs, upon their first perihelion passage, produce more CO<sub>2</sub> than CO compared to dynamically old LPCs after several visits to the inner Solar System, consistent with previous smaller surveys of solar system comets (A’Hearn et al. 2012; Ootsubo et al. 2012). Harrington Pinto et al. (2022) posited that CO is depleted in dynamically new LPCs from galactic cosmic rays altering the surface layers of ices resulting in an overall higher CO<sub>2</sub>/CO mixing ratios during their first passage in the inner Solar System (Gronoff et al. 2020; Maggilo et al. 2020).

The energy from galactic cosmic rays (GCR) can be deposited down to a depth of  $\sim 70$  meters into the surface of a comet depending on the bulk properties of the comet and the energy of the GCRs Gronoff et al. (2020). Maggilo et al. (2020) argued that sufficiently high energy GCRs alter the chemical composition of cometary surface ices via radiolysis of H<sub>2</sub>O, CO, and CO<sub>2</sub> down to  $\sim 10$ – $20$  meters. In a similar analysis for 3I/ATLAS, Maggilo et al. (2025) estimated GCR conversion of CO to CO<sub>2</sub> down to a depth of  $\sim 15$ – $20$  meters to explain the unusually large CO<sub>2</sub>/CO mixing ratio measured with JWST pre-perihelion observations (Cordiner et al. 2025). They also estimated pre-perihelion erosion of the surface of 3I/ATLAS to be less than  $\sim 1$  meter and up to a few tens of meters near perihelion passage. Therefore, they concluded that it is unlikely the erosion of the surface of 3I/ATLAS would reveal deeper layers of pristine material. The erosion of the nucleus we estimate in this work of  $\sim 1.05$ – $6.56$  meters is consistent with these previous estimates. In the future, observations of deeper layers of an interstellar comet may reveal more

primordial compositions. This may be possible with a trajectory that spends more time in the inner Solar System, a smaller interstellar object, or an in-situ measurement.

## 6 CONCLUSIONS

Here we summarize the main results presented in this paper:

(i) Equations (10), (12), (14), (23), (25), and (27) provide a methodology to estimate the final nuclear radius of a small body undergoing mass loss for an arbitrary trajectory and mass loss function.

(ii) We compiled all measured production rates of 3I/ATLAS and provide a table of these measurements and the associated heliocentric distances, observation dates, facility/instrument, and citation.

(iii) We perform conservative and optimistic fits of observed production rates as a function of pre- and post-perihelion positions of 3I/ATLAS. We fit production rates for nine and seven different chemical species detected in the coma from pre- and post-perihelion observations, respectively.

(iv) The total estimated mass loss of 3I/ATLAS from fits of the production rates to be  $\sim 10^9\text{--}10^{10}$  kg.

(v) Assuming an initial radius of  $\sim 1.3$  km, we approximate the erosion of the surface of 3I/ATLAS to be down to a depth of  $\sim 1.05\text{--}6.56$  meters.

(vi) Based on these mass loss and radius change estimate we conclude that it is unlikely that the surface has been eroded down to layers of unaltered material. In consideration of reported abundances, we maintain that surface erosion has nonetheless revealed layers that provide insights into the post-formation processing history of the comet.

## ACKNOWLEDGEMENTS

DZS acknowledges funding support from JWST GO 5959, which was provided by NASA through a grant from the Space Telescope Science Institute. We thank Adina Feinstein and Cassidy Walker for useful conversations.

*Software:* matplotlib (Hunter 2007), numpy (Harris et al. 2020), scipy (Virtanen et al. 2020).

## DATA AVAILABILITY

The machine readable table of production rates utilized in this publication is available at this link: [🔗](#).

## REFERENCES

A'Hearn M. F., et al., 2012, *ApJ*, **758**, 29  
 Ahuja G., Ganesh S., 2026, *Research Notes of the American Astronomical Society*, **10**, 19  
 Al Mawla R., Cœur C., Houzel N., Billet S., Gaudion V., Romanias M. N., 2025, *Atmospheric Environment*, **354**, 121260  
 Alvarez-Candal A., Rizos J. L., Lara L. M., Santos-Sanz P., Gutierrez P. J., Ortiz J. L., Morales N., 2025, *A&A*, **700**, L10  
 Aravind K., Ganesh S., Venkataramani K., Sahu D., Angchuk D., Sivarani T., Unni A., 2021, *MNRAS*, **502**, 3491  
 Bagnulo S., et al., 2021, *Nature Communications*, **12**, 1797  
 Bannister M. T., et al., 2020, arXiv e-prints, p. arXiv:2001.11605  
 Belyakov M., et al., 2025, *Research Notes of the American Astronomical Society*, **9**, 194

Belyakov M., Wong I., Bolin B. T., Ryleigh Davis M., Bromley S. J., Lisse C. M., Brown M. E., 2026, arXiv e-prints, p. arXiv:2601.22034  
 Beniama J., 2025, *PASJ*, **77**, L71  
 Bergner J. B., Seligman D. Z., 2023, *Nature*, **615**, 610  
 Biver N., et al., 2026, arXiv e-prints, p. arXiv:2603.23240  
 Bodewits D., et al., 2020, *Nature Astronomy*, **4**, 867  
 Borisov G., et al., 2019, Central Bureau Electronic Telegrams, 4666, 1  
 Chandler C. O., et al., 2025, arXiv e-prints, p. arXiv:2507.13409  
 Choi S., et al., 2026, arXiv e-prints, p. arXiv:2601.08591  
 Combi M. R., Mäkinen T., Bertaux J.-L., Quemerais E., Ferron S., Lallement R., Schmidt W., 2025, arXiv e-prints, p. arXiv:2512.22354  
 Cordiner M. A., et al., 2020, *Nature Astronomy*, **4**, 861  
 Cordiner M. A., et al., 2025, *ApJ*, **991**, L43  
 Cordiner M., et al., 2026, arXiv e-prints, p. arXiv:2603.06911  
 Coulson I. M., et al., 2025, arXiv e-prints, p. arXiv:2510.02817  
 Cremonese G., et al., 2020, *ApJ*, **893**, L12  
 Deam S. E., et al., 2025, arXiv e-prints, p. arXiv:2507.05051  
 Denneau L., Siverd R., Tonry J., Weiland H., Erasmus N., Fitzsimmons A., Robinson J., 2025, MPEC  
 Eubanks T. M., et al., 2025a, arXiv e-prints, p. arXiv:2508.15768  
 Eubanks T. M., et al., 2025b, *Research Notes of the American Astronomical Society*, **9**, 324  
 Feinstein A. D., Noonan J. W., Seligman D. Z., 2025, *ApJ*, **991**, L2  
 Ferrin I., et al., 2026, arXiv e-prints, p. arXiv:2604.09941  
 Fitzsimmons A., et al., 2018, *Nature Astronomy*, **2**, 133  
 Fitzsimmons A., et al., 2019, *ApJ*, **885**, L9  
 Forbes J. C., Butler H., 2026, *Research Notes of the American Astronomical Society*, **10**, 12  
 Frincke T. T., et al., 2026, *MNRAS*, **545**, staf1994  
 Gerakines P. A., Yarnall Y. Y., Hudson R. L., 2024, *Icarus*, **413**, 116007  
 Gillan A. F., et al., 2026, arXiv e-prints, p. arXiv:2603.01383  
 Giorgini J., et al., 2015, NASA JPL Horizons On-Line Ephemeris System, <https://ssd.jpl.nasa.gov/horizons/manual.html>  
 Grant S. R., Jones G. H., 2025, *Research Notes of the American Astronomical Society*, **9**, 276  
 Gray Z., et al., 2025, *ApJ*, **992**, L29  
 Gronoff G., et al., 2020, *ApJ*, **890**, 89  
 Guo Y., Zhang L., Feng F., Li Z.-Y., Pomazan A., Yang X., 2025, *AJ*, **170**, 362  
 Guzik P., Drahus M., 2021, *Nature*, **593**, 375  
 Guzik P., Drahus M., Rusek K., Waniak W., Cannizzaro G., Pastor-Marazuela I., 2020, *Nature Astronomy*, **4**, 53  
 Harrington Pinto O., Womack M., Fernandez Y., Bauer J., 2022, *Planet. Sci. J.*, **3**, 247  
 Harris C. R., et al., 2020, *Nature*, **585**, 357  
 Hartman J. D., et al., 2026, arXiv e-prints, p. arXiv:2602.21586  
 Helbert J., Rauer H., Boice D. C., Huebner W. F., 2005, *A&A*, **442**, 1107  
 Hinkle J. T., Yang B., Meech K. J., Hoffman A., Shappee B. J., Hoogendam W. B., Wray J. J., 2025, arXiv e-prints, p. arXiv:2512.02106  
 Hoogendam W. B., et al., 2025a, arXiv e-prints, p. arXiv:2510.11779  
 Hoogendam W. B., et al., 2025b, arXiv e-prints, p. arXiv:2512.09020  
 Hoogendam W. B., et al., 2026, arXiv e-prints, p. arXiv:2601.16983  
 Hopkins M. J., Dorsey R. C., Forbes J. C., Bannister M. T., Lintott C. J., Leicester B., 2025, *ApJ*, **990**, L30  
 Hui M.-T., Ye Q.-Z., Föhning D., Hung D., Tholen D. J., 2020, *AJ*, **160**, 92  
 Hui M.-T., Jewitt D., Mutchler M. J., Agarwal J., Kim Y., 2026, arXiv e-prints, p. arXiv:2601.21569  
 Hunter J. D., 2007, *Computing in Science & Engineering*, **9**, 90  
 Hutsemékers D., et al., 2026a, arXiv e-prints, p. arXiv:2605.07652  
 Hutsemékers D., et al., 2026b, *A&A*, **706**, A43  
 Jacobson-Bell B., Croft S., White E., Siemion A. P. V., Lebofsky M., MacMahon D. H. E., 2025, *Research Notes of the American Astronomical Society*, **9**, 351  
 Jewitt D., 2009, *AJ*, **137**, 4296  
 Jewitt D., Luu J., 2019, *ApJ*, **886**, L29  
 Jewitt D., Luu J., 2025, *ApJ*, **994**, L3  
 Jewitt D., Luu J., Rajagopal J., Kotulla R., Ridgway S., Liu W., Augusteijn T., 2017, *The Astrophysical Journal Letters*, **850**, L36

- Jewitt D., Hui M.-T., Mutchler M., Kim Y., Agarwal J., 2025, *ApJ*, **990**, L2
- Kareta T., et al., 2020, *ApJ*, **889**, L38
- Kareta T., et al., 2025, *ApJ*, **990**, L65
- Keto E., Loeb A., 2026, *MNRAS*, **545**, staf2054
- Kim Y., Jewitt D., Mutchler M., Agarwal J., Hui M.-T., Weaver H., 2020, *ApJ*, **895**, L34
- Kushwaha R. K., Gudipati M. S., Henderson B. L., 2025, *ApJ*, **987**, 190
- Li J., Shi X., Hui M.-T., Shi J., 2026a, *arXiv e-prints*, p. [arXiv:2602.14218](#)
- Li J.-K., Tao Z.-Z., Zhang T.-J., 2026b, *arXiv e-prints*, p. [arXiv:2603.19023](#)
- Lin H. W., Lee C.-H., Gerdes D. W., Adams F. C., Becker J., Napier K., Markwardt L., 2020, *ApJ*, **889**, L30
- Linstrom P., Mallard W., 2001,
- Lisse C. M., et al., 2025a, *arXiv e-prints*, p. [arXiv:2512.07318](#)
- Lisse C. M., et al., 2025b, *Research Notes of the American Astronomical Society*, **9**, 242
- Lisse C. M., et al., 2026, *arXiv e-prints*, p. [arXiv:2601.06759](#)
- Lucas S., Ferry D., Demirdjian B., Suzanne J., 2005, *Journal of Physical Chemistry B*, **109**, 18103
- Maggiolo R., et al., 2020, *ApJ*, **901**, 136
- Maggiolo R., Dhooghe F., Gronoff G., de Keyser J., Cessateur G., 2025, *arXiv e-prints*, p. [arXiv:2510.26308](#)
- Manfroid J., Hutsemékers D., Jehin E., 2021, *Nature*, **593**, 372
- Martinez-Palomera J., Tuson A., Hedges C., Dotsion J., Barclay T., Powell B., 2025, *ApJ*, **994**, L51
- Martinez-Palomera J., Tuson A., TESS Science Support Center 2026, *Research Notes of the American Astronomical Society*, **10**, 28
- McKay A. J., Cochran A. L., Dello Russo N., DiSanti M. A., 2020, *ApJ*, **889**, L10
- Medler K., et al., 2026, *arXiv e-prints*, p. [arXiv:2602.23586](#)
- Meech K. J., et al., 2017, *Nature*, **552**, 378
- Micheli M., et al., 2018, *Nature*, **559**, 223
- Monk H., Seligman D. Z., 2026, *arXiv e-prints*, p. [arXiv:2602.04806](#)
- Ootsubo T., et al., 2012, *ApJ*, **752**, 15
- Opitom C., et al., 2019, *A&A*, **631**, L8
- Opitom C., et al., 2025, *MNRAS*, **544**, L31
- Opitom C., et al., 2026, *arXiv e-prints*, p. [arXiv:2603.07187](#)
- Paek G. S. H., et al., 2026, *arXiv e-prints*, p. [arXiv:2602.12930](#)
- Pérez-Couto X., Torres S., Villaver E., Mustill A. J., Manteiga M., 2025, *arXiv e-prints*, p. [arXiv:2509.07678](#)
- Puzia T. H., Rahatgaonkar R., Carvajal J. P., Nayak P. K., Luco B., 2025, *ApJ*, **990**, L27
- Rahatgaonkar R., et al., 2025, *ApJ*, **995**, L34
- Ren X., et al., 2026, *arXiv e-prints*, p. [arXiv:2603.10350](#)
- Roth N. X., et al., 2025, *arXiv e-prints*, p. [arXiv:2511.20845](#)
- Roth N. X., et al., 2026, *arXiv e-prints*, p. [arXiv:2603.20445](#)
- Salazar Manzano L. E., et al., 2025, *ApJ*, **993**, L23
- Salazar Manzano L. E., et al., 2026, *Nature Astronomy*,
- Santana-Ros T., et al., 2025, *A&A*, **702**, L3
- Seligman D. Z., et al., 2025, *ApJ*, **989**, L36
- Serra-Ricart M., Licandro J., Alarcon M. R., 2025, *arXiv e-prints*, p. [arXiv:2512.12819](#)
- Sheikh S. Z., et al., 2025, *arXiv e-prints*, p. [arXiv:2512.18142](#)
- Shinnaka Y., Tsujimoto K., Kawakita H., Kobayashi H., Watanabe J.-i., Ootsubo T., 2026, *arXiv e-prints*, p. [arXiv:2603.25002](#)
- Spada F., Królikowska M., Dones L., 2026, *arXiv e-prints*, p. [arXiv:2603.00782](#)
- Tan H., Yan X., Li J.-Y., 2026, *arXiv e-prints*, p. [arXiv:2601.15443](#)
- Taylor A. G., Seligman D. Z., 2025, *ApJ*, **990**, L14
- Tonry J. L., et al., 2018, *PASP*, **130**, 064505
- Tonry J. L., et al., 2025, *ApJ*, **995**, L15
- Trigo-Rodríguez J. M., Gritsevich M., Blum J., 2025, *arXiv e-prints*, p. [arXiv:2511.19112](#)
- Virtanen P., et al., 2020, *Nature Methods*, **17**, 261
- Williams G. V., Sato H., Sarneczky K., Wainscoat R., Woodworth D., Meech K., 2017, *Central Bureau Electronic Telegrams*, **4450**, 1
- Xing Z., Bodewits D., Noonan J., Bannister M. T., 2020, *ApJ*, **893**, L48
- Xing Z., Oset S., Noonan J., Bodewits D., 2025, *ApJ*, **991**, L50
- Yaginuma A., Taylor A. G., Seligman D. Z., 2025a, *arXiv e-prints*, p. [arXiv:2510.25945](#)
- Yaginuma A., Frincke T., Seligman D. Z., Mandt K., DellaGiustina D. N., Peña-Asensio E., Taylor A. G., Nolan M. C., 2025b, *ApJ*, **995**, 64
- Yang B., et al., 2021, *Nature Astronomy*
- Yang B., Meech K. J., Connelley M., Zhao R., Keane J. V., 2025, *ApJ*, **992**, L9
- Ye Q.-Z., Zhang Q., Kelley M. S. P., Brown P. G., 2017, *ApJ*, **851**, L5
- Ye Q., et al., 2025, *ApJ*, **993**, L31
- Zhang Q., Battams K., 2026, *PASP*, **138**, 014403
- Zhao R., Zhang X., Yang B., Fan X., Wang S., Huang Y., Liu J., 2026, *arXiv e-prints*, p. [arXiv:2603.07718](#)
- de la Fuente Marcos R., et al., 2025, *A&A*, **700**, L9

## APPENDIX A: EXPANDED TABLE

In this appendix we provide Table A1, which contains every reported production rate for 3I/ATLAS to date.

**Table A1:** Catalog of production rates for chemical species  $Q_X$  from observations of 3I/ATLAS. Includes error associated with  $Q_X$ , observation dates, heliocentric distance  $r_H$ , facility used to obtained observation, and relevant citation. Error of zero indicates the production rate is an upper limit and those with three dots indicate a repeated entry. Note that the errors are of the same order of magnitude as the corresponding value of  $Q_X$ .

Volatile	Production Rate [ $s^{-1}$ ]	Error [ $s^{-1}$ ]	Observation Date	$r_H$ [au]	Facility	Reference
H <sub>2</sub> O	$9.10 \times 10^{26}$	0.00	07/04/25–05/26/25	4.47	X-SHOOTER	<a href="#">Alvarez-Candal et al. (2025)</a>
	$7.40 \times 10^{26}$	0.50	07/31/25 – 08/01/25	3.51	UVOT	<a href="#">Xing et al. (2025)</a>
	$3.20 \times 10^{26}$	0.20	08/01/25–08/15/25	3.20	SPHEREx	<a href="#">Lisse et al. (2025b)</a>
	$1.07 \times 10^{26}$	0.08	08/06/25	3.32	JWST	<a href="#">Cordiner et al. (2025)</a>
	$1.36 \times 10^{27}$	0.50	08/18/25–08/20/25	2.90	UVOT	<a href="#">Xing et al. (2025)</a>
	$9.46 \times 10^{27}$	0.00	08/26/25–09/03/25	2.54	TMRT	<a href="#">Li et al. (2026a)</a>
	$1.45 \times 10^{28}$	0.52	09/08/25–09/09/25	2.27	...	...
	$2.08 \times 10^{28}$	0.41	09/18/25–09/23/25	1.96	...	...
	$5.00 \times 10^{24}$	2.00	11/01/25–11/3/25	1.36–1.37	IRAM	<a href="#">Biver et al. (2026)</a>
	$1.60 \times 10^{29}$	0.20	11/04/25	1.37	ALMA /ACA	<a href="#">Salazar Manzano et al. (2026)</a>
	$3.17 \times 10^{29}$	0.04	11/06/25	1.40	SOHO/SWAN	<a href="#">Combi et al. (2025)</a>
	$2.31 \times 10^{29}$	0.03	11/09/25	1.42	...	...
	$2.35 \times 10^{29}$	0.04	11/10/25	1.43	...	...
	$2.36 \times 10^{29}$	0.04	11/12/25	1.44	...	...
	$3.94 \times 10^{28}$	1.30	11/13/25	1.46	...	<a href="#">Tan et al. (2026)</a>
	$2.45 \times 10^{29}$	0.04	11/13/25	1.46	...	<a href="#">Combi et al. (2025)</a>
	$2.09 \times 10^{29}$	0.04	11/14/25	1.47	...	...
	$5.15 \times 10^{28}$	1.65	11/15/25	1.48	...	<a href="#">Tan et al. (2026)</a>
	$2.19 \times 10^{29}$	0.04	11/15/25	1.48	...	<a href="#">Combi et al. (2025)</a>
	$4.23 \times 10^{28}$	1.37	11/16/25	1.50	...	<a href="#">Tan et al. (2026)</a>
	$1.91 \times 10^{29}$	0.04	11/16/25	1.50	...	<a href="#">Combi et al. (2025)</a>
	$3.34 \times 10^{28}$	1.07	11/17/25	1.51	...	<a href="#">Tan et al. (2026)</a>
	$3.92 \times 10^{28}$	1.27	11/18/25	1.53	...	<a href="#">Tan et al. (2026)</a>
	$2.51 \times 10^{29}$	0.04	...	1.55	...	<a href="#">Combi et al. (2025)</a>
	$3.29 \times 10^{29}$	0.49	11/19/25	1.56	...	...
	$2.19 \times 10^{29}$	0.04	11/20/25	1.84	...	...
	$2.55 \times 10^{28}$	1.08	11/25/25	1.66	...	<a href="#">Tan et al. (2026)</a>
	$1.83 \times 10^{28}$	0.66	11/26/25	1.68	...	...
	$1.42 \times 10^{29}$	0.04	...	1.68	...	<a href="#">Combi et al. (2025)</a>
	$4.08 \times 10^{28}$	0.07	12/02/25	1.84	...	...
	$2.46 \times 10^{28}$	0.76	12/03/25	1.85	...	<a href="#">Tan et al. (2026)</a>
	$7.60 \times 10^{27}$	0.27	...	1.85	...	<a href="#">Combi et al. (2025)</a>
	$1.55 \times 10^{28}$	0.66	12/04/25	1.87	...	<a href="#">Tan et al. (2026)</a>
	$2.43 \times 10^{28}$	0.10	...	1.87	...	<a href="#">Combi et al. (2025)</a>
	$1.88 \times 10^{28}$	0.66	12/05/25	1.89	...	<a href="#">Tan et al. (2026)</a>
	$1.14 \times 10^{28}$	0.22	...	1.91	...	<a href="#">Combi et al. (2025)</a>
	$1.30 \times 10^{28}$	0.45	12/06/25	1.92	...	<a href="#">Tan et al. (2026)</a>
	$3.68 \times 10^{28}$	0.08	...	1.92	...	<a href="#">Combi et al. (2025)</a>
	$1.26 \times 10^{28}$	0.51	12/07/25	1.95	...	<a href="#">Tan et al. (2026)</a>
	$2.04 \times 10^{28}$	0.14	...	1.95	SOHO/SWAN	<a href="#">Combi et al. (2025)</a>
	$1.50 \times 10^{28}$	0.54	12/08/25	1.98	...	<a href="#">Tan et al. (2026)</a>
	$1.40 \times 10^{28}$	0.28	12/08/25–12/15/25	2.00–2.20	SPHEREx	<a href="#">Lisse et al. (2026)</a>
	$1.00 \times 10^{28}$	0.25	12/09/25	1.99	SWAN-SOHO	<a href="#">Combi et al. (2025)</a>
	$1.60 \times 10^{28}$	0.13	12/10/25	2.01	...	...
	$1.13 \times 10^{28}$	0.42	12/15/25	2.17	...	<a href="#">Tan et al. (2026)</a>
	$1.13 \times 10^{28}$	0.48	12/16/25	2.19	...	<a href="#">Tan et al. (2026)</a>
	$3.35 \times 10^{28}$	0.07	12/15/25–12/16/25	2.19–2.20	JWST/MIRI	<a href="#">Belyakov et al. (2026)</a>
	$1.28 \times 10^{28}$	0.47	12/17/25	2.22	SOHO/SWAN	<a href="#">Tan et al. (2026)</a>
	$1.70 \times 10^{28}$	0.00	12/22/25	2.37	ALMA /ACA	<a href="#">Cordiner et al. (2026)</a>
	$8.47 \times 10^{28}$	0.05	...	2.37	JWST	<a href="#">Roth et al. (2026)</a>
$9.82 \times 10^{28}$	0.13	12/23/25	2.39	JWST	<a href="#">Roth et al. (2026)</a>	
$1.61 \times 10^{28}$	0.01	12/22/25–12/23/25	2.40	JWST/NIRSpec	...	
$8.85 \times 10^{28}$	0.12	12/27/25	2.54	JWST/MIRI	<a href="#">Belyakov et al. (2026)</a>	

CO <sub>2</sub>	$9.50 \times 10^{26}$	0.05	08/06/25	3.32	JWST	Cordiner et al. (2025)
	$1.60 \times 10^{27}$	0.10	08/01/25–08/15/25	3.20	SPHEREx	Lisse et al. (2025b)
	$3.00 \times 10^{27}$	0.45	12/08/25–12/15/25	2.00–2.20	SPHEREx	Lisse et al. (2026)
	$1.06 \times 10^{28}$	0.02	12/15/25	2.19–2.20	JWST/MIRI	Belyakov et al. (2026)
	$6.44 \times 10^{27}$	0.12	12/27/25	2.54	...	Belyakov et al. (2026)
	$3.94 \times 10^{27}$	0.01	12/22/25–12/23/25	2.40	JWST/NIRSpec	Cordiner et al. (2026)
CO	$1.10 \times 10^{27}$	0.00	07/18/25–07/21/25	3.92 – 3.84	JCMT	Hinkle et al. (2025)
	$1.70 \times 10^{26}$	0.04	08/06/25	3.32	JWST	Cordiner et al. (2025)
	$1.00 \times 10^{26}$	0.25	08/01/25–08/15/25	3.10 – 3.30	SPHEREx	Lisse et al. (2025b)
	$5.75 \times 10^{27}$	1.91	09/07/25–09/29/25	2.01	TMRT	Li et al. (2026a)
	$6.80 \times 10^{27}$	0.11	11/01/25–11/03/25	1.36–1.37	IRAM	Biver et al. (2026)
	$7.60 \times 10^{27}$	0.45	12/08/25–12/15/25	2.00–2.20	SPHEREx	Lisse et al. (2026)
	$2.64 \times 10^{27}$	0.01	12/22/25	2.37	ALMA /ACA	Cordiner et al. (2026)
	$3.50 \times 10^{27}$	0.02	12/23/25	2.39	JWST	Roth et al. (2026)
CN	$5.60 \times 10^{24}$	0.00	07/02/25	4.47	TTT	de la Fuente Marcos et al. (2025)
	$5.60 \times 10^{23}$	0.00	07/04/25–07/05/25	4.41	X-SHOOTER	Alvarez-Candal et al. (2025)
	$9.80 \times 10^{23}$	0.00	07/12/25	4.14	SNIFS	Hoogendam et al. (2025a)
	$3.89 \times 10^{24}$	1.04	07/27/25	3.65	X-SHOOTER	Rahatgaonkar et al. (2025)
	$5.80 \times 10^{24}$	1.09	08/10/25	3.16	MDM	Salazar Manzano et al. (2025)
	$1.70 \times 10^{24}$	1.99	08/12/25	3.14	UVES	Rahatgaonkar et al. (2025)
	$4.82 \times 10^{24}$	0.34	...	3.14	MDM	Salazar Manzano et al. (2025)
	$1.58 \times 10^{24}$	1.99	...	3.14	UVES	Hutsemékers et al. (2026b)
	$3.89 \times 10^{24}$	1.12	08/15/25	3.04	...	Rahatgaonkar et al. (2025)
	$3.89 \times 10^{24}$	1.12	...	3.04	...	Hutsemékers et al. (2026b)
	$6.34 \times 10^{24}$	0.29	08/16/25	2.97	MDM	Salazar Manzano et al. (2025)
	$7.17 \times 10^{24}$	0.38	...	2.94	...	...
	$8.40 \times 10^{23}$	3.20	08/18/25	2.94	SNIFS	Hoogendam et al. (2025a)
	$1.20 \times 10^{24}$	0.30	08/23/25	2.79	SNIFS	Hoogendam et al. (2025a)
	$1.70 \times 10^{24}$	0.50	08/24/25	2.75	KCWI	Hoogendam et al. (2025b)
	$5.70 \times 10^{24}$	1.50	08/27/25	2.66	LRIS	Medler et al. (2026)
	$6.16 \times 10^{24}$	1.10	08/28/25	2.64	UVES	Hutsemékers et al. (2026b)
	$6.50 \times 10^{24}$	0.50	09/02/25	2.48	SNIFS	Hoogendam et al. (2025a)
	$9.12 \times 10^{24}$	1.07	09/3/25–09/4/25	2.44	UVES	Hutsemékers et al. (2026b)
	$1.07 \times 10^{25}$	1.02	09/10/25	2.25	...	...
	$2.19 \times 10^{25}$	1.02	09/11/25	2.22	...	...
	$2.88 \times 10^{25}$	1.02	09/12/25	2.19	...	...
	$2.69 \times 10^{25}$	1.02	09/14/25	2.14	...	...
	$4.07 \times 10^{25}$	1.05	09/20/25	1.97	X-SHOOTER	...
	$5.01 \times 10^{25}$	1.05	09/22/25	1.92	...	...
	$5.25 \times 10^{25}$	1.05	09/23/25	1.90	...	...
	$5.37 \times 10^{25}$	1.05	09/24/25	1.87	...	...
	$5.37 \times 10^{25}$	1.05	09/25/25	1.85	...	...
	$1.60 \times 10^{25}$	0.50	11/16/25	1.50	KCWI	Hoogendam et al. (2026)
	$3.20 \times 10^{25}$	1.20	11/30/25	1.79	SNIFS	Medler et al. (2026)
	$2.18 \times 10^{25}$	1.05	12/02/25	1.85	BFOSC	Zhao et al. (2026)
	$3.31 \times 10^{25}$	1.05	12/04/25	1.89	YFOSC	...
	$3.09 \times 10^{25}$	1.05	12/06/25	1.95	...	...
	$3.16 \times 10^{25}$	1.05	12/07/25	1.97	...	...
	$1.95 \times 10^{25}$	1.05	12/17/25	2.25	...	...
	$2.75 \times 10^{25}$	1.07	12/19/25	2.31	...	...
	$1.45 \times 10^{25}$	1.15	12/20/25	2.33	BFOSC	...
	$1.26 \times 10^{25}$	1.15	12/23/25	2.42	...	...
	$3.10 \times 10^{24}$	0.60	12/22/25–12/23/25	2.40	JWST/NIRSpec	Cordiner et al. (2026)
	$8.91 \times 10^{24}$	1.15	12/26/25	2.51	BFOSC	Zhao et al. (2026)
$8.91 \times 10^{24}$	1.05	12/28/25	2.57	YFOSC	...	
$6.03 \times 10^{24}$	1.07	1/11/26	3.00	...	...	
$4.37 \times 10^{24}$	1.07	1/20/26	3.29	...	...	
HCN	$1.70 \times 10^{24}$	0.00	07/16/25–07/17/25	4.01 –3.97	JCMT	Hinkle et al. (2025)
	$1.50 \times 10^{25}$	0.00	08/07/25	3.29	JCMT	Coulson et al. (2025)
	$2.10 \times 10^{25}$	0.00	08/15/25	3.00	...	...
	$1.70 \times 10^{25}$	0.00	08/22/25	2.8	...	...

	$1.40 \times 10^{25}$	0.00	08/28/25	2.81	...	...
	$1.10 \times 10^{25}$	0.00	09/03/25	2.63	...	...
	$1.20 \times 10^{25}$	0.50	09/07/25	2.33	...	...
	$5.00 \times 10^{24}$	0.01	09/12/25	2.17	ALMA /ACA	Roth et al. (2026)
	$4.00 \times 10^{24}$	0.01	09/12/25	2.17	ALMA /ACA	Roth et al. (2026)*
	$4.00 \times 10^{25}$	1.70	09/14/25	2.14	JCMT	Coulson et al. (2025)
	$1.00 \times 10^{25}$	0.01	09/15/25	2.11	ALMA /ACA	Roth et al. (2026)
	$9.00 \times 10^{24}$	0.01	09/15/25	2.11	ALMA /ACA	Roth et al. (2026)*
	$4.13 \times 10^{25}$	0.20	11/01/25–11/03/25	1.36–1.37	IRAM	Biver et al. (2026)
	$6.75 \times 10^{24}$	0.54	12/22/25	2.37	ALMA /ACA	Cordiner et al. (2026)
OH	$8.20 \times 10^{26}$	0.00	07/04/25–05/26/25	4.41	X-SHOOTER	Alvarez-Candal et al. (2025)
	$1.48 \times 10^{26}$	0.00	07/27/25	3.14	UVES	Rahatgaonkar et al. (2025)
	$3.80 \times 10^{26}$	1.10	08/28/25	2.64	...	Hutsemékers et al. (2026b)
	$6.16 \times 10^{26}$	1.05	09/03/25–09/04/25	2.44	...	...
	$1.74 \times 10^{27}$	1.35	09/10/25	2.25	...	...
	$2.14 \times 10^{27}$	1.26	09/12/25	2.19	...	...
Ni	$1.62 \times 10^{22}$	1.35	07/23/25	3.78	X-SHOOTER	Rahatgaonkar et al. (2025)
	$1.29 \times 10^{22}$	1.62	...	3.78	X-SHOOTER	Hutsemékers et al. (2026b)
	$2.24 \times 10^{22}$	1.62	07/27/25	3.65	...	...
	$2.69 \times 10^{22}$	1.15	07/30/25	3.55	...	...
	$6.76 \times 10^{22}$	1.04	08/09/25	3.23	...	...
	$6.60 \times 10^{22}$	1.05	08/12/25	3.14	UVES	...
	$6.76 \times 10^{22}$	1.17	08/14/25	3.07	X-SHOOTER	...
	$5.49 \times 10^{22}$	1.20	08/15/25	3.04	UVES	...
	$8.13 \times 10^{22}$	1.15	08/16/25	3.01	X-SHOOTER	...
	$1.20 \times 10^{23}$	1.15	08/21/25	2.85	...	...
	$1.99 \times 10^{22}$	1.17	...	2.85	X-SHOOTER	Rahatgaonkar et al. (2025)
	$1.86 \times 10^{23}$	1.12	08/28/25	2.64	UVES	Hutsemékers et al. (2026b)
	$3.23 \times 10^{23}$	1.09	09/03/25–09/04/25	2.44	...	...
	$5.62 \times 10^{23}$	1.07	09/10/25	2.25	...	...
	$6.30 \times 10^{23}$	1.07	09/12/25	2.19	...	...
	$1.12 \times 10^{24}$	1.12	09/20/25	1.97	X-SHOOTER	...
	$1.78 \times 10^{24}$	1.10	09/22/25	1.92	...	...
	$1.99 \times 10^{24}$	1.10	09/23/25	1.90	...	...
	$1.95 \times 10^{24}$	1.01	09/24/25	1.87	...	...
	$2.04 \times 10^{24}$	1.01	09/25/25	1.85	...	...
	$6.61 \times 10^{24}$	2.74	11/16/25	1.50	KCWI	Hoogendam et al. (2026)
	$9.77 \times 10^{24}$	1.05	12/02/25	1.85	BFOSC	Zhao et al. (2026)
	$8.71 \times 10^{24}$	1.23	12/04/25	1.89	YFOSC	...
	$7.76 \times 10^{24}$	1.23	12/06/25	1.95	...	...
	$9.12 \times 10^{23}$	1.07	12/06/25	1.93	UVES	Hutsemékers et al. (2026a)
	$6.76 \times 10^{24}$	1.23	12/07/25	1.97	YFOSC	Zhao et al. (2026)
	$9.33 \times 10^{23}$	1.10	12/10/25	2.04	UVES	Hutsemékers et al. (2026a)
	$7.78 \times 10^{23}$	1.07	12/15/25	2.18	...	...
	$5.01 \times 10^{24}$	1.23	12/17/25	2.25	YFOSC	Zhao et al. (2026)
	$3.63 \times 10^{24}$	1.23	12/19/25	2.31	...	...
	$4.7 \times 10^{24}$	1.05	12/20/25	2.33	BFOSC	...
	$6.16 \times 10^{23}$	1.10	12/21/25	2.35	UVES	Hutsemékers et al. (2026a)
	$3.98 \times 10^{24}$	1.05	12/23/25	2.42	BFOSC	Zhao et al. (2026)
	$3.39 \times 10^{24}$	1.05	12/26/25	2.51	...	...
	$1.15 \times 10^{24}$	1.10	...	2.19	JWST/MIRI	Belyakov et al. (2026)
	$4.57 \times 10^{23}$	1.10	12/26/25	2.50	UVES	Hutsemékers et al. (2026a)
	$2.88 \times 10^{24}$	1.23	12/28/25	2.57	YFOSC	Zhao et al. (2026)
	$1.82 \times 10^{23}$	1.12	01/11/26	2.99	UVES	Hutsemékers et al. (2026a)
	$1.95 \times 10^{24}$	1.23	...	3.00	YFOSC	Zhao et al. (2026)
	$1.14 \times 10^{23}$	1.15	01/19/26	3.24	UVES	Hutsemékers et al. (2026a)
	$1.51 \times 10^{24}$	1.23	01/20/26	3.29	YFOSC	Zhao et al. (2026)
	$7.59 \times 10^{22}$	1.17	01/27/26	3.50	UVES	Hutsemékers et al. (2026a)
	$2.75 \times 10^{22}$	1.26	02/07/26	3.85	...	...
Fe	$1.00 \times 10^{22}$	1.20	08/28/25	2.64	UVES	Hutsemékers et al. (2026b)
	$4.00 \times 10^{22}$	1.10	09/03/25–09/04/25	2.44	...	...

	$1.15 \times 10^{23}$	1.07	09/10/25	2.25	...	...
	$1.58 \times 10^{23}$	1.05	09/12/15	2.19	...	...
	$4.78 \times 10^{23}$	1.07	09/20/25	1.97	X-SHOOTER	...
	$8.51 \times 10^{23}$	1.07	09/22/25	1.92	...	...
	$1.00 \times 10^{24}$	1.05	09/23/25	1.90	...	...
	$1.15 \times 10^{24}$	1.07	09/24/25	1.87	...	...
	$1.17 \times 10^{24}$	1.07	09/25/25	1.85	...	...
	$9.55 \times 10^{24}$	3.96	11/16/25	1.50	KCWI	<a href="#">Hoogendam et al. (2026)</a>
	$2.09 \times 10^{24}$	1.10	12/04/25	1.88	UVES	<a href="#">Hutsemékers et al. (2026a)</a>
	$8.32 \times 10^{23}$	1.02	12/06/25	1.93	...	...
	$8.51 \times 10^{23}$	1.02	12/10/25	2.04	...	...
	$6.03 \times 10^{23}$	1.02	12/15/25	2.18	...	...
	$3.16 \times 10^{23}$	1.02	12/21/25	2.35	...	...
	$1.86 \times 10^{23}$	1.02	12/26/25	2.50	...	...
	$4.27 \times 10^{22}$	1.10	01/11/26	2.99	...	...
	$2.29 \times 10^{22}$	1.17	01/19/26	3.24	...	...
	$1.38 \times 10^{22}$	1.50	01/27/26	3.50	...	...
C <sub>2</sub>	$3.98 \times 10^{24}$	1.58	08/28/25	2.64	UVES	<a href="#">Hutsemékers et al. (2026b)</a>
	$3.98 \times 10^{24}$	1.58	09/03/25–09/04/25	2.44	...	...
	$3.71 \times 10^{24}$	1.05	09/10/25	2.25	...	...
	$4.78 \times 10^{24}$	1.12	09/12/25	2.19	...	...
	$1.74 \times 10^{25}$	1.12	09/22/25	1.92	X-SHOOTER	...
	$2.09 \times 10^{25}$	1.12	09/23/25	1.9	...	...
	$2.57 \times 10^{25}$	1.12	09/24/25	1.87	...	...
	$2.57 \times 10^{25}$	1.12	09/25/25	1.85	...	...
	$8.80 \times 10^{25}$	0.80	11/16/25	1.5	KCWI	<a href="#">Hoogendam et al. (2026)</a>
	$6.46 \times 10^{24}$	1.05	12/02/25	1.85	BFOSC	<a href="#">Zhao et al. (2026)</a>
	$6.31 \times 10^{24}$	1.23	12/04/25	1.89	YFOSC	...
	$5.75 \times 10^{24}$	1.23	12/06/25	1.95	...	...
	$4.79 \times 10^{24}$	1.23	12/07/25	1.97	...	...
	$2.00 \times 10^{24}$	1.23	12/17/25	2.25	...	...
	$1.48 \times 10^{24}$	1.23	12/19/25	2.31	...	...
	$1.48 \times 10^{24}$	1.07	12/20/25	2.33	BFOSC	...
	$8.32 \times 10^{23}$	1.07	12/23/25	2.42	...	...
	$5.50 \times 10^{23}$	1.23	12/28/25	2.57	YFOSC	...
CH <sub>3</sub> OH	$5.00 \times 10^{25}$	0.60	08/28/25	2.64	ALMA /ACA	<a href="#">Roth et al. (2026)</a>
	$8.00 \times 10^{26}$	1.00	09/18/25	2.03	ALMA /ACA	<a href="#">Roth et al. (2026)*</a>
	$9.60 \times 10^{26}$	0.70	09/18/25	2.03	ALMA /ACA	<a href="#">Roth et al. (2026)</a>
	$1.21 \times 10^{26}$	0.50	09/22/2025	1.92	ALMA /ACA	<a href="#">Roth et al. (2026)</a>
	$2.29 \times 10^{27}$	0.40	10/01/25	1.71	ALMA /ACA	<a href="#">Roth et al. (2026)</a>
	$3.38 \times 10^{27}$	0.05	11/01/25–11/03/25	1.36–1.37	IRAM	<a href="#">Biver et al. (2026)</a>
	$4.10 \times 10^{27}$	0.10	11/04/25	1.37	ALMA /ACA	<a href="#">Salazar Manzano et al. (2026)</a>
	$1.37 \times 10^{27}$	0.04	12/23/25	2.39	JWST/NIRSpec	<a href="#">Roth et al. (2026)</a>
<sup>13</sup> CO <sub>2</sub>	$1.30 \times 10^{25}$	0.25	08/01/25–08/12/25	3.20	...	<a href="#">Lisse et al. (2025b)</a>
	$9.40 \times 10^{24}$	0.00	12/22/25–12/23/25	2.40	JWST/NIRSpec	<a href="#">Cordiner et al. (2026)</a>
OCS	$8.90 \times 10^{23}$	2.00	08/06/25	3.32	JWST	<a href="#">Cordiner et al. (2025)</a>
	$5.00 \times 10^{26}$	0.00	11/01/25–11/03/25	1.36–1.37	IRAM	<a href="#">Biver et al. (2026)</a>
	$4.70 \times 10^{24}$	0.11	12/22/25–12/23/25	2.40	JWST/NIRSpec	<a href="#">Cordiner et al. (2026)</a>
C <sub>3</sub>	$5.00 \times 10^{24}$	0.40	11/16/25	1.50	KCWI	<a href="#">Hoogendam et al. (2026)</a>
misc. organics	$2.00 \times 10^{27}$	0.28	12/08/25–12/15/25	2.0–2.20	SPHEREx	<a href="#">Lisse et al. (2026)</a>
CH <sub>4</sub>	$4.60 \times 10^{26}$	0.20	12/15/25–12/16/25	2.19–2.20	JWST/MIRI	<a href="#">Belyakov et al. (2026)</a>
	$1.90 \times 10^{26}$	0.02	12/23/25	2.39	JWST/NIRSpec	<a href="#">Roth et al. (2026)</a>
	$2.40 \times 10^{26}$	0.20	12/27/25	2.54	...	<a href="#">Belyakov et al. (2026)</a>
HDO	$1.21 \times 10^{27}$	0.00	11/01/25–11/3/25	1.36–1.37	IRAM	<a href="#">Biver et al. (2026)</a>
	$1.50 \times 10^{27}$	0.20	11/04/25	1.37	ALMA /ACA	<a href="#">Salazar Manzano et al. (2026)</a>
CH <sub>3</sub> CN	$1.50 \times 10^{25}$	0.40	11/01/25–11/03/25	1.36–1.37	IRAM	<a href="#">Biver et al. (2026)</a>
H <sub>2</sub> CO	$3.50 \times 10^{26}$	0.40	11/01/25–11/03/25	1.36–1.37	IRAM	<a href="#">Biver et al. (2026)</a>
	$3.90 \times 10^{24}$	0.90	12/23/15	2.39	JWST/NIRSpec	<a href="#">Roth et al. (2026)</a>
H <sub>2</sub> S	$3.90 \times 10^{26}$	0.00	11/01/25–11/03/25	1.36–1.37	IRAM	<a href="#">Biver et al. (2026)</a>
CS	$1.70 \times 10^{25}$	0.40	11/01/25–11/30/25	1.36–1.37	IRAM	<a href="#">Biver et al. (2026)</a>

HC <sub>3</sub> N	$2.10 \times 10^{25}$	0.00	11/01/25–11/03/25	1.36–1.37	IRAM	<a href="#">Biver et al. (2026)</a>
CH <sub>3</sub> CHO	$1.40 \times 10^{26}$	0.70	11/01/25–11/03/25	1.36–1.37	IRAM	<a href="#">Biver et al. (2026)</a>
(CH <sub>3</sub> OH) <sub>2</sub>	$3.30 \times 10^{26}$	1.30	11/01/25–11/03/25	1.36–1.37	IRAM	<a href="#">Biver et al. (2026)</a>
SO	$2.70 \times 10^{26}$	0.00	11/01/25–11/03/25	1.36–1.37	IRAM	<a href="#">Biver et al. (2026)</a>
HCNO	$2.50 \times 10^{26}$	0.11	11/01/25–11/03/25	1.36–1.37	IRAM	<a href="#">Biver et al. (2026)</a>
HCOOH	$1.09 \times 10^{27}$	0.00	11/01/25–11/03/25	1.36–1.37	IRAM	<a href="#">Biver et al. (2026)</a>
NH <sub>2</sub> CHO	$2.80 \times 10^{25}$	0.00	11/01/25–11/03/25	1.36–1.37	IRAM	<a href="#">Biver et al. (2026)</a>
CH <sub>3</sub> OD	$1.79 \times 10^{26}$	0.00	11/01/25–11/03/25	1.36–1.37	IRAM	<a href="#">Biver et al. (2026)</a>
CH <sub>3</sub> D	$2.50 \times 10^{25}$	0.30	12/23/25	2.39	JWST	<a href="#">Roth et al. (2026)</a>
C <sub>2</sub> H <sub>6</sub>	$2.00 \times 10^{25}$	0.20	12/23/25	2.39	JWST	<a href="#">Roth et al. (2026)</a>

This paper has been typeset from a  $\text{\TeX}/\text{\LaTeX}$  file prepared by the author.